Millimeter-wave optical double resonance schemes for rapid assignment of perturbed spectra, with applications to the [~ over C] [superscript 1]B[subscript 2] state of SO[subscript 2]

Millimeter-wave optical double resonance schemes for rapid assignment of perturbed spectra, with applications to the $\tilde{C}\ ^1B_2$ state of SO_2

G. Barratt Park,[1,a)] Caroline C. Womack,[1] Andrew R. Whitehill,[2] Jun Jiang,[1] Shuhei Ono,[2] and Robert W. Field[1,b)]

[1]*Department of Chemistry, Massachusetts Institute of Technology, Cambridge, Massachusetts 02139, USA*
[2]*Department of Earth, Atmospheric, and Planetary Sciences, Massachusetts Institute of Technology, Cambridge, Massachusetts 02139, USA*

(Received 16 January 2015; accepted 22 March 2015; published online 10 April 2015)

Millimeter-wave detected, millimeter-wave optical double resonance (mmODR) spectroscopy is a powerful tool for the analysis of dense, complicated regions in the optical spectra of small molecules. The availability of cavity-free microwave and millimeter wave spectrometers with frequency-agile generation and detection of radiation (required for chirped-pulse Fourier-transform spectroscopy) opens up new schemes for double resonance experiments. We demonstrate a multiplexed population labeling scheme for rapid acquisition of double resonance spectra, probing multiple rotational transitions simultaneously. We also demonstrate a millimeter-wave implementation of the coherence-converted population transfer scheme for background-free mmODR, which provides a ~10-fold sensitivity improvement over the population labeling scheme. We analyze perturbations in the $\tilde{C}$ state of SO_2, and we rotationally assign a b_2 vibrational level at 45 328 cm^{-1} that borrows intensity via a *c*-axis Coriolis interaction. We also demonstrate the effectiveness of our multiplexed mmODR scheme for rapid acquisition and assignment of three predissociated vibrational levels of the $\tilde{C}$ state of SO_2 between 46 800 and 47 650 cm^{-1}. [http://dx.doi.org/10.1063/1.4916908]

I. INTRODUCTION

The $\tilde{C}$ ($^1B_2$) state of SO_2 has attracted considerable attention from spectroscopists, dynamicists, and theorists. The origin at $\nu_{0\text{–}0} = 42\,573.45$ cm^{-1} is close in energy to the onset of dissociation into ground state $SO(^3\Sigma^-) + O(^3P)$ at ~45 725 cm^{-1}.[1] Thus, the $\tilde{C}$ state plays an important role in the photodissociation of SO_2 in the earth's atmosphere. However, there is evidence for more than one dissociation mechanism, including vibronic coupling to the dissociation continuum of the ground $\tilde{X}$ electronic state,[2–4] intersystem crossing to one or more dissociative triplet states,[1,5–7] and a singlet mechanism due to avoided crossing with the dissociative 3 $^1A'$ state.[8,9] It is likely that all three mechanisms contribute, and that the relative contribution depends on the energy.[10,11]

The $\tilde{C}$ state potential energy surface (PES) has an unusual structure around equilibrium. There is a double-minimum potential in the q_3 antisymmetric stretch coordinate with a barrier of ~141 cm^{-1} at the C_{2v} geometry.[12] The global minimum of the PES is doubly degenerate and has a C_s equilibrium geometry with non-equivalent SO bond lengths of ~1.491 and 1.639 Å.[12] There is considerable indirect evidence for staggering in the $(v_1', v_2', v_3') = (0, 0, v_3')$ progression that reflects the presence of the barrier,[12–14] but direct observation of b_2 vibrational levels (with odd quanta of v_3') has not previously been made because transitions to b_2 vibrational levels of the $\tilde{C}$ state are forbidden from the vibrationless level of the $\tilde{X}\ ^1A_1$ ground electronic state. There have been observations of dispersed fluorescence from $\tilde{C}$-state levels around 47 620–50 570 cm^{-1} of excitation, terminating on $\tilde{X}$-state levels of b_2 vibrational symmetry,[8,15] which indicates a_1/b_2 vibrational admixture at 5000–8000 cm^{-1} of vibrational excitation in the $\tilde{C}$-state. Brand *et al.*[15] have attributed the admixture to rotation-vibration interaction via *c*-axis Coriolis matrix elements, but Ray *et al.*[8] have argued that the admixture is due to vibronic interaction with the dissociative 3 $^1A'$ state. Here, we report the first direct observation and rotational assignment of a b_2 vibrational level of the $\tilde{C}$ state, which borrows intensity via *c*-axis Coriolis interaction, and we provide a note of caution about interpreting the interaction mechanism in the absence of rotational assignments.

Above the dissociation threshold, the laser-induced fluorescence (LIF) intensities from the $\tilde{C}$ state fall off rapidly, although the Franck-Condon absorption intensity envelope continues to increase.[3] The strongest band in the LIF spectrum of SO_2 occurs at 45 335 cm^{-1}, approximately 100 cm^{-1} below the dissociation threshold. However, due to perturbations in the rotational structure, only a handful of rotational levels were assigned in the jet-cooled LIF spectra of Yamanouchi *et al.*[16] This band was originally assigned the vibrational quantum numbers (v_1', v_2', v_3') = "(1, 3, 2)," but subsequent analysis[4] suggested that this normal mode quantum number assignment is not physically meaningful, so in our discussion, we will label this vibrational level "B_{a_1}." In the current work, we use the perturbed region surrounding this level to demonstrate

a)Electronic addresses: barratt@mit.edu and barratt.park@gmail.com
b)Electronic mail: rwfield@mit.edu

the effectiveness of various millimeter-wave optical double resonance (mmODR) schemes, and we report a rotational analysis of the region surrounding the perturbed band.

The use of free induction decay (FID)-detected, mmODR schemes greatly simplify the analysis of perturbed band structures. When monitoring millimeter-wave transitions of the ground state, mmODR information can be used for unambiguous identification of the lower level involved in the optical transition, because a double resonance signal indicates that the millimeter-wave transition and the optical transition share a common level. The frequency-agility of our chirped-pulse millimeter wave (CPmmW) spectrometer,[17] based on the Pate design,[18,19] allows us to perform multiplexed mmODR, where more than one millimeter-wave transition is monitored simultaneously, and we demonstrate the effectiveness of multiplexed mmODR schemes for rapid acquisition and rotational assignment of three predissociated levels of the $\tilde{C}$ state of SO_2 between 46 800 and 47 650 cm^{-1}. We have also made a millimeter-wave implementation of the background free coherence-converted population transfer (CCPT) technique.[20–22] We find that CCPT provides an excellent improvement in signal-to-noise over traditional population labeling schemes, and is a promising alternative to polarization-based background-free double-resonance methods.[23] However, there are challenges to implementing the technique in our current experimental configuration, where the coherent experiment must be completed in a time window that is short compared to the millimeter-wave Doppler lifetime of <2 μs. In Sec. II, we discuss the advantages of various double-resonance schemes.

II. EXPERIMENTAL DETAILS

A. Millimeter-wave optical double resonance configuration

The mmODR spectra were obtained in a vacuum chamber equipped with a spectrometer designed originally for CPmmW experiments. The CPmmW spectrometer is described in Ref. 17, so we will omit the details here. The UV radiation was generated by a pulsed dye laser (Lambda Physik FL3002E), operating with Coumarin 440 dye, pumped by the 355 nm third harmonic of an Nd:YAG laser (Spectra-Physics DCR-3). The dye laser output was frequency-doubled in a β-barium borate crystal. A small portion of the fundamental was passed through a heated $^{130}Te_2$ vapor cell for frequency calibration. An intracavity etalon reduced the spectral width to 0.04 cm^{-1}. An unskimmed molecular jet of neat SO_2 was expanded through a pulsed valve (General Valve, Series 9, d = 1 mm) at a backing pressure of 2 atm.

The geometry used for the double resonance experiment is shown schematically in Figure 1. The millimeter-wave beam was focused by a matched set of 20 cm diameter polytetrafluoroethylene (PTFE) lenses ($f \approx 30$ cm). The UV laser beam was expanded to match the millimeter-wave beam waist, which had a diffraction-limited diameter of approximately 2.5 cm. The laser beam was propagated counter to the molecular jet, and the millimeter waves were propagated at a 90° angle. The E-field of the focused millimeter-wave beam was ~42 V/m and the UV power was ~300 μJ/pulse.

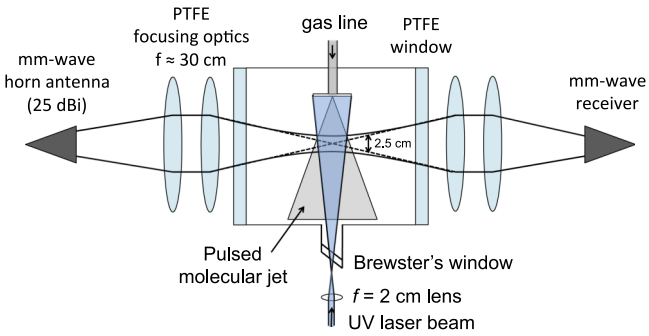

FIG. 1. Schematic drawing of the experimental configuration used for the mmODR experiments. Our primary geometric consideration was to optimize the spatial overlap of the molecular, optical, and millimeter wave beams in the interaction region, since any portion of the molecular jet that overlaps with the millimeter waves, but *not* the optical pulse will contribute to background signal, but not to double-resonance signal. Thus, we focus the millimeter wave beam to its diffraction limit, and we expand the optical beam to match.

Both the UV laser and the millimeter waves were vertically polarized.

B. Available schemes for millimeter-wave optical double resonance

Microwave detected, microwave optical double resonance (MODR) was first demonstrated by Nakajima *et al.*[24] The authors of Ref. 24 pointed out two possible timing schemes for MODR experiments in which microwave FID is detected (see Figure 2). In the following discussion, we will use a simplified version of the optical Bloch picture in the rotating frame, assuming that the driving pulse is on resonance, and ignoring dephasing effects. With these assumptions, the driving vector, $\mathbf{\Omega}$, lies along the x-axis with magnitude equal to the Rabi frequency, $|\mathbf{\Omega}| = \mu_{ab}\mathcal{E}/\hbar$. The dynamics of the Bloch vector, $\mathbf{\Theta}$, due to the microwave radiation are given by $d\mathbf{\Theta}/dt = \mathbf{\Omega} \times \mathbf{\Theta}$ so that the Bloch vector lies in the y,z plane. The z component is proportional to the population difference of the two level system and the y component is proportional to the coherent polarization. As pointed out by Neill *et al.*,[22] the Bloch sphere picture is not a completely accurate description of rotational transitions because there are multiple degenerate M_J subcomponents with different transition moments, but it a useful model for qualitative discussion of double-resonance schemes.

In Case 1 (top panel of Figure 2), the optical excitation comes before the microwave pulse. In this double-resonance case, the optical pulse depletes either (1) the lower level of the microwave transition or (2) the upper level of the microwave transition, which leads, respectively, to (1) a decrease in population difference between the levels of the microwave transition and a decrease in microwave signal or (2) an increase in population difference between the levels of the microwave transition and an increase in the microwave signal. Thus, Case 1 is a population-labeling scheme, in which the sign of the double resonance signal corresponds to whether the optical transition is connected to the upper or lower level of the microwave transition.

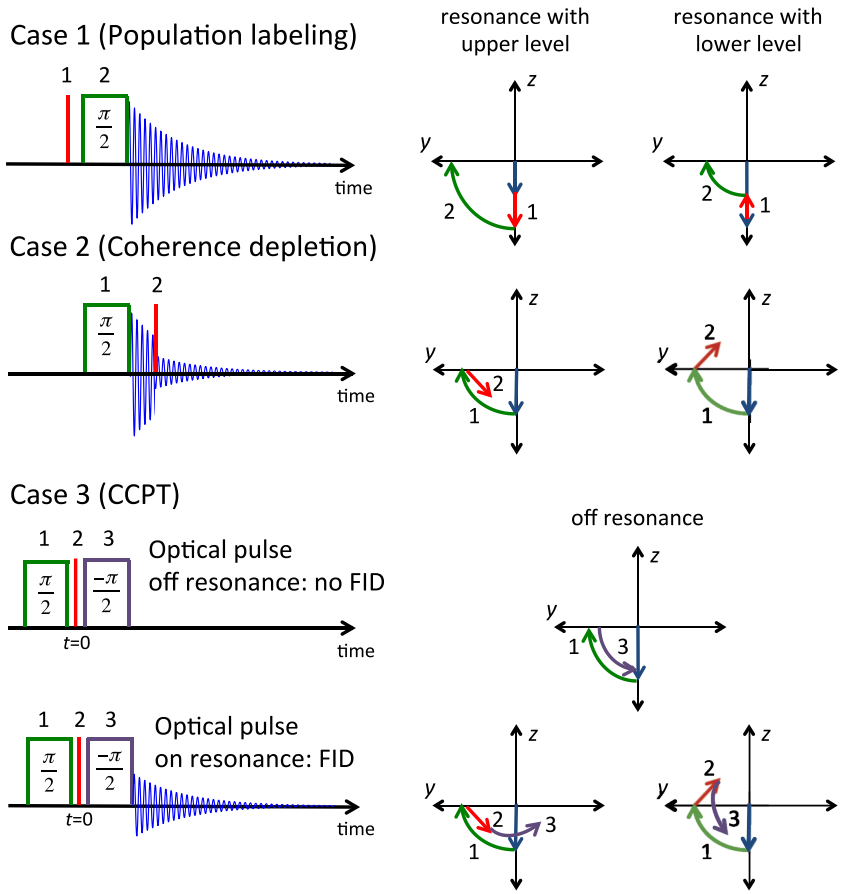

FIG. 2. Schematic comparison of three FID-detected MODR schemes, reported in Refs. 20–22 and 24. The left-hand side of the figure shows the timing sequence. Microwave pulses are labeled "$\pi/2$" or "$-\pi/2$" to indicate the relative phase. The optical pulse is represented by a red line and the FID is represented by a blue decaying signal. The right-hand side of the figure shows a simplified schematic of the optical Bloch vector treatment for each FID-detected MODR case. The behavior of the Bloch vector is shown for an optical resonance with both the upper and lower levels of the microwave transitions. The z-axis represents the population difference $\rho_{aa}-\rho_{bb}$ between the levels involved in the microwave transition, and the y-axis is related to the coherence, $y = i(\rho_{ab}-\rho_{ba})$. For our schematic purposes, we ignore time evolution of the coherence, so we omit the x-axis ($x = \rho_{ab}+\rho_{ba}$).

In Case 2 (middle panel of Figure 2), the optical excitation comes after the microwave pulse. In this double resonance scheme, the optical photon has no effect on the initial population difference between the levels of the microwave transition. Instead, the optical pulse removes population of coherently radiating molecules regardless of whether the resonance is with the upper or lower level of the microwave transition. In Case 2, the double resonance signal is always negative. Note that in this case, the effect of the optical pulse contributes both a z (population) and y (coherence) component to the Bloch vector. We see that this is the case from density matrix considerations. If a and b are the coefficients of the upper and lower states in the microwave transition, respectively, then an optical resonance with the upper level will lead to a decrease in the magnitude of $|a|$, leading to a decrease in the z-component of the Bloch vector, $\rho_{aa} - \rho_{bb} = aa^* - bb^*$ *and* a decrease in the magnitude of the coherence, $|\rho_{ab}| = |ab^*|$. However, since the optical pulse comes later than the microwave pulse, the double resonance signal is only related to the depletion of the coherence.

The authors of Ref. 24 argue that in Case 1, a >50% depletion of FID signal is not possible, but that in Case 2, a >50% depletion can be obtained. However, we believe that the first clause of this argument—which would be true for most optically detected double resonance experiments—is incorrect for *microwave detected* MODR. In a typical microwave experiment (even when run under jet-cooled conditions) $h\nu \ll kT$, so the initial population difference is typically on the order of a few percent or less. On the other hand, the upper level in the optical transition is negligibly populated, so a saturated optical absorption may deplete 50% of the *population* from one of the lower levels involved in the microwave transition. Since the FID signal is proportional to the initial population *difference* for the microwave transition, which is small, it is not only possible to deplete the FID signal by >50% in Case 1—in our experience, it is possible to remove enough population from the lower level of the microwave transition as to cause a population inversion between the lower levels, which will result in a 2nd derivative-type double resonance lineshape. For our purposes, we prefer Case 1 for strong double resonance signals because of the convenient population labeling. However, when the double-resonance signal is weak relative to pulse-to-pulse signal fluctuation, Case 2 provides an advantage because background signal fluctuations can largely be corrected by taking the ratio of FID intensity before and after the laser pulse. Case 2 might also provide an advantage when the rotational structure is not fully resolved because signal from the two levels of the microwave transition will add instead of cancel.

A third type of MODR scheme known as CCPT was developed more recently by the research groups of B. H. Pate and his collaborators.[20–22] The technique is made possible by taking advantage of phase-coherent excitation and detection of the microwave FID. CCPT is a three-pulse sequence. The

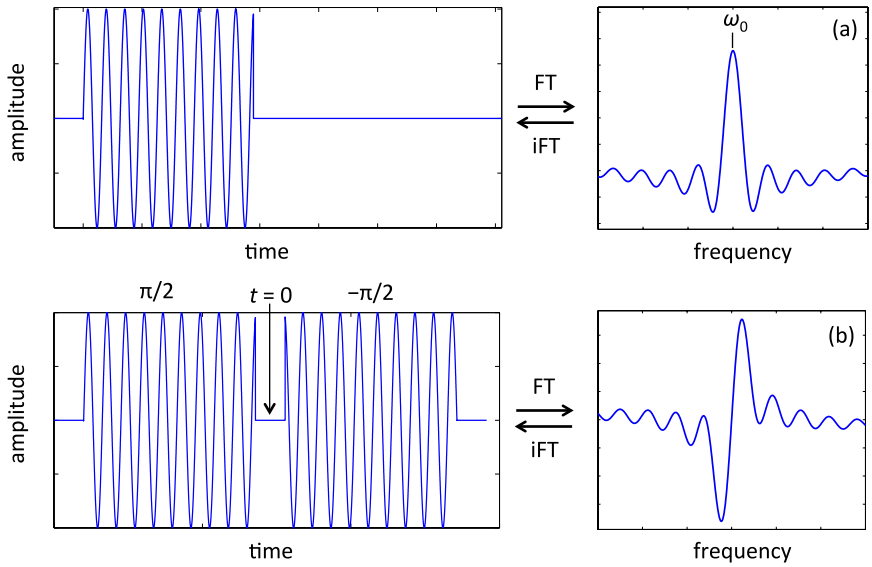

FIG. 3. A windowed sine pulse has a frequency domain spectrum with power centered at the carrier frequency, ω_0, and an envelope determined by the window function (panel (a)). In CCPT, the "$\pi/2$" sine pulse is followed by a "$-\pi/2$" sine pulse. This combined waveform has even parity, but there is no cosine component at the ω_0 carrier frequency. The Fourier transform is purely real and crosses through zero at ω_0, but will contain an envelope centered at the carrier frequency, whose shape is determined by the window function (panel (b)). The Fourier transform must regenerate the original time-domain waveform when the inverse Fourier transform is applied.

first "$\pi/2$" microwave pulse generates a coherence. A second "$-\pi/2$" microwave pulse with the same pulse area but *opposite* phase cancels the coherence.

An optical pulse interacts with the molecules at $t = 0$, *between* the two microwave pulses. The optical pulse removes population from one of the microwave levels. This will cause a z-axis component to be added to the Bloch vector (an accompanying loss of coherence will also occur). A positive z-axis component will be added if the laser is resonant with the lower level and a negative z-axis component will be added if the laser is resonant with the upper level. The result is that when the laser is resonant with one of the levels in the microwave transition, the $-\pi/2$ rotation of the Bloch vector by the second microwave pulse no longer cancels the coherence. Furthermore, the phase of the resulting FID is sensitive to whether the optical pulse was resonant with the upper or lower level of the microwave transition. Because the method is background free, there is a significant sensitivity advantage for Case 3, relative to Cases 1 and 2.

While CCPT is very effective for monitoring optical resonances connected to individual rotational lines excited by a single-frequency pulse, the technique is *incompatible* with chirped excitation schemes, where a broadband chirped pulse is used to multiplex the collection of double resonance information for a number of rotational transitions simultaneously. We believe there is some confusion about this point in the spectroscopy community, so we discuss it briefly. In order to null the FID using a "$\pi/2$" and "$-\pi/2$" pulse scheme, one must choose the correct relative phase of the "$-\pi/2$" pulse. The phase that will null the FID is the phase for which the magnitude Fourier transform of the two pulses, taken collectively, cancels at the resonance frequency, ω_0, because the net effect is that in the absence of optical double resonance, the two pulse sequence transfers no power into the microwave transition. For the Fourier transform magnitude to be zero at ω_0, the real and imaginary components must both be zero. In other words, the ω_0 sine component of the two individual pulses must *collectively* create an even parity waveform and the ω_0 cosine component of the two individual pulses must collectively create an odd parity waveform. An example of such a pulse is shown in Figure 3(b). (We have arbitrarily chosen to use a sine pulse, so that the time-domain waveform has even parity.) The Fourier transform of this two-pulse sequence will be zero at the resonance frequency, but must contain a window function intensity pattern centered at the carrier frequency, which will re-generate the original waveform when the inverse Fourier transform is applied. If we were to add a contribution from another frequency located arbitrarily nearby (at $\omega_0 + \delta\omega$), it would be impossible to cancel the Fourier transform magnitude at both frequencies simultaneously. The only windowed (non-infinite in duration) continuous time-domain function for which the *all* sine contributions and *all* cosine contributions vanish over a continuous range is the trivial solution $f(t) = 0$.

The frequency-domain waveform shown in Figure 3(a) has the familiar form, $F(\omega) \propto \mathrm{sinc}(\omega - \omega_0)$. We can correctly predict the shape of the frequency-domain CCPT waveform shown in Figure 3(b) by a simplified analysis that neglects the time gap between the "$\pi/2$" and "$-\pi/2$" pulses. The time-domain waveform can then be written,

$$f(t) = \sin(\omega_0 t) R(t) S(t), \tag{1}$$

where $R(t)$ is a rectangular window function that envelopes the two-pulse sequence and $S(t)$ is the sign function,

$$S(t) = \begin{cases} -1 & \text{if } t < 0 \\ +1 & \text{if } t > 0 \end{cases}. \tag{2}$$

In Eq. (1), $S(t)$ is responsible for ensuring that the "$-\pi/2$" pulse is 180° out of phase with the "$\pi/2$" pulse. The Fourier transform of $S(t)$ has the form $\mathcal{F}[S(t)] \propto 1/\omega$. Therefore, by the convolution theorem, the Fourier transform of Eq. (1) has a form proportional to the convolution of $\mathrm{sinc}(\omega - \omega_0)$ with $1/\omega$. This convolution will have most of its intensity near the peak of the sinc function at ω_0, but passes through zero at the resonance frequency due to the odd parity of $\mathcal{F}[S(t)] \propto 1/\omega$. Within an inhomogeneously broadened transition, molecules with offsets $+\delta\omega$ and $-\delta\omega$ from the center frequency, ω_0, will be driven with equal magnitude but opposite phase. Since the $T_2 = 1/\Delta\omega$ decay is on the same timescale as the $1/2\delta\omega$ beat

recovery, most of the inhomogeneous emission excited by the CCPT pulse will cancel.

C. Implementation of millimeter-wave optical double resonance schemes

In our double resonance experiments, we have tried several different schemes. First, we have implemented a variant of Case 1 in which the millimeter-wave pulse probes multiple different ground state transitions simultaneously (upper panel of Figure 4). Double resonances with the various ground state transitions are easily resolved because the Fourier transform detection method distinguishes different frequency components of the FID. This scheme is multiplexed, so that as the laser is scanned, double resonances with multiple different ground-state rotational levels are observed simultaneously. This scheme was first considered by the B. H. Pate group at the University of Virginia,[25] but to our knowledge, the scheme has not been discussed in the published literature, so we provide a brief description. In cases (such as the $\tilde{C}$ state of SO_2) where the double-resonance signals are strong, but the LIF spectrum is difficult to assign due to perturbations and congestion, this scheme provides an incredible advantage, because the population labeling provides automatic rotational assignment of the LIF spectrum *in a single scan* of the laser through the band. In conventional non-multiplexed double resonance techniques, the laser must be scanned across the band many times, once for each ground state transition used in the double resonance scheme. Because our millimeter-wave spectrometer operates in the power-limited regime, we obtain the best signal when we drive each ground state microwave transition with a typically ~50–100 ns single-frequency rectangular pulse. The rectangular pulses are applied sequentially in the time domain so that the total time required to polarize five ground state microwave transitions (providing double-resonance information for up to ten rotational levels) is 250–500 ns.

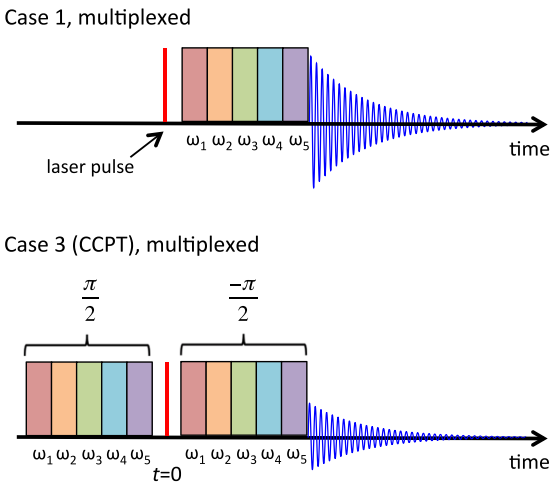

FIG. 4. In the absence of a Fabry-Perot cavity, the FID-detected MODR schemes shown in Figure 2 may be multiplexed for the simultaneous acquisition of double-resonance information from many different microwave transitions. Schematic timing sequences are shown for multiplexed implementations of Case 1 and Case 3. Each excitation pulse contains a sequence of single-frequency rectangular pulses, which each polarize a different microwave transition. The double-resonance signal at each frequency is obtained from the Fourier transform of the FID.

We have also made a millimeter-wave implementation of the background-free CCPT technique, which significantly improved the sensitivity of our double-resonance experiment by at least an order of magnitude. Unlike the CCPT implementation described in Refs. 20–22, we do not employ a cavity, so our quality factor is unity ($Q = 1$) and we have access to a broad range of frequencies in each pulse. We therefore attempted a multiplexed implementation of CCPT using a series of single-frequency pulses, as shown in the bottom panel of Figure 4. This scheme works so long as the single frequency pulses are resolved and the window functions of each frequency component (Figure 3(b)) do not overlap. The phase of each "$-\pi/2$" frequency was tuned empirically to minimize the off-resonant FID. We found this multiplexed CCPT scheme to be challenging in our experimental configuration because the transverse Doppler dephasing time in our unskimmed jet is approximately 2 μs at 70 GHz. Because of its coherent nature, the *entire* CCPT experiment (including both sets of microwave pulses and the FID detection) must be carried out in a time that is short relative to 2 μs. When the amount of time between the "$\pi/2$" and "$-\pi/2$" pulses for a given frequency approaches the Doppler dephasing time, we observe a metamorphosis of the signal type from Case 3 to Case 1 (because the transition begins to lose memory of the first "$\pi/2$" pulse). Furthermore, because our spectrometer is power-limited by the current availability of broadband millimeter-wave amplifiers, we lose signal by using shorter excitation pulses.[17] Therefore, we prefer to use the multiplexed implementation of Case 1 when the double-resonance signals are strong because it provides rapid rotational assignment of the LIF spectrum (for many values of $J''_{K''_a K''_c}$) in a single scan of the laser. However, when greater sensitivity is desired, such as in our detection of levels that perturb the $\tilde{C}(B_{a_1})$ state of SO_2, we prefer to use the non-multiplexed CCPT scheme (Case 3). Sample spectra obtained using the millimeter-wave CCPT implementation are shown in Figure 5. The sensitivity improvement over our Case 1 implementation is at least an order of magnitude although the acquisition time is longer because the laser must be scanned through the band once for each ground state microwave transition. We provide a direct comparison with the multiplexed Case 1 spectrum in Fig. S1 of the supplementary material.[26]

We briefly mention alternative schemes that may allow multiplexed implementation of background-free double resonance. One approach would be to change the experimental geometry so that the millimeter-waves propagate along the molecular beam axis. This can be accomplished using a rooftop reflector as described in Ref. 17. In this geometry, the Doppler dephasing time is an order of magnitude longer and it will be much easier to perform coherent experiments in less time than the Doppler dephasing. There are experimental difficulties involved in overlapping the optical pulse in the rooftop reflector configuration, which we are currently working to resolve.

Another idea for multiplexed background-free mmODR is to use a polarization scheme such as the millimeter-wave

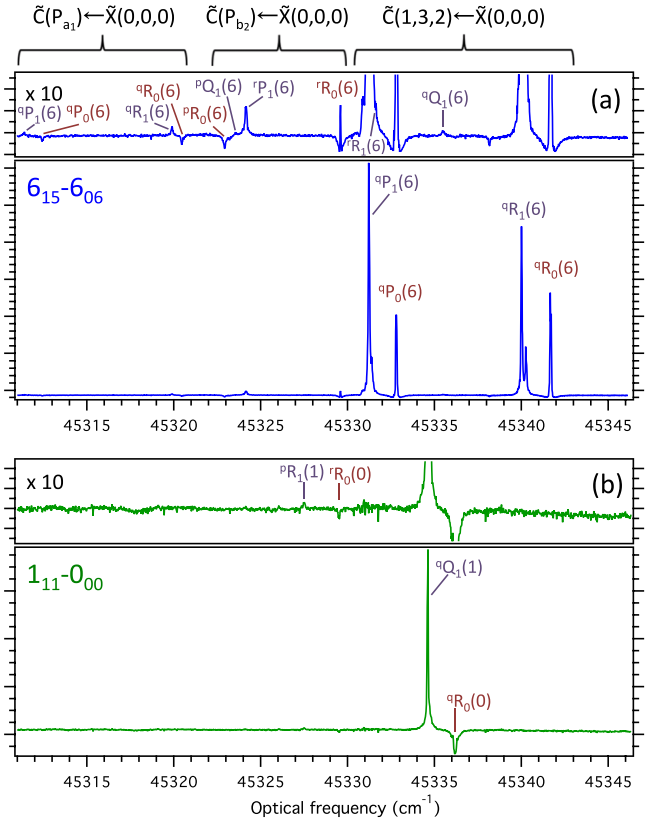

FIG. 5. Sample mmODR spectra obtained using our millimeter-wave implementation of the CCPT scheme, showing the sensitivity of the technique. Panel (a) shows a double-resonance spectrum acquired using the $J''_{K''_aK''_c} = 6_{15}$–$6_{06}$ microwave transition and panel (b) shows a spectrum acquired using the 1_{11}–0_{00} microwave transition. The signal obtained for the bright $\tilde{C}(B_{a_1}) \leftarrow \tilde{X}(0,0,0)$ transition is very strong (roughly 100:1 signal:background noise). The insets show a 10× vertical magnification and transitions to perturbing levels are evident.

detected, millimeter-wave optical polarization spectroscopy (mmOPS) used by Steeves *et al.*[23] In this scheme, the millimeter-wave source and receiver are cross polarized at 90° so that in the absence of double resonance, no signal reaches the detector. An optical pulse polarized at 45° to the millimeter-wave source and receiver alters the M''_J distribution when it is brought into resonance with the one of the lower levels. This effectively rotates the polarization of the FID, allowing it to reach the detector. In the original implementation,[23] millimeter-wave power was detected noncoherently using a bolometer, but there is nothing that should prevent the technique being used for coherent multiplexed Fourier transform detection. Steeves *et al.* report a fourfold improvement in sensitivity in their bolometer-detected experiment. This is less than the sensitivity advantage of CCPT because CCPT is sensitive to the *total* population transfer (ignoring coherence losses) whereas mmOPS is only sensitive to the *relative* population transfer out of different M_J levels.

III. RESULTS

A. Perturbations in the $\tilde{C}(B_{a_1})$ level

The rotational structure of the C̃-state vibrational level at 45 335 cm^{-1} (originally given the assignment, (v'_1, v'_2, v'_3) = "(1, 3, 2)," but which we label "B_{a_1}") is severely perturbed. In the analysis of the high-resolution LIF spectrum, Yamanouchi *et al.*[16] assign only six term values, and they report an effective C constant that is greater than the effective B constant, presumably due to a pathological c-axis Coriolis perturbation. Assignment of the perturbed spectrum is further complicated by the fact that the B constant of SO_2 is small enough that many features in the LIF spectrum of the supersonic expansion at ~10 K rotational temperature are not fully resolved.

We applied the multiplexed Case 1 mmODR scheme to the B_{a_1} level. From a single multiplexed mmODR scan, we are almost able to triple the number of assigned term values, due to the simultaneous rotational assignments afforded by the multiplexed technique. (See the Appendix and Figure 6.) We followed up with more sensitive CCPT scans, probing a single ground-state rotational transition at a time. Figure 5 provides a sample of two CCPT spectra of the region surrounding the B_{a_1} level. Transitions to two perturbing vibrational levels are evident. The primary perturber, "P_{b_2}," is a level of b_2 vibrational symmetry that borrows intensity from B_{a_1} via a c-axis Coriolis interaction. The Coriolis interaction lends much greater (~10×) intensity to the transitions from $J'' = 6$ (Fig. 5(a)) than to the transitions from $J'' = 0$ or 1 (Fig. 5(b))—the latter set of transitions is barely visible above the background noise. There is an additional set of weak transitions at the low-frequency end of Figure 5(a). This appears to be from a Franck-Condon weak transition to a level of a_1 vibrational symmetry, which we call "P_{a_1}," and which interacts with P_{b_2} via a c-axis Coriolis matrix element. The vibrational structure of the C̃ state is perturbed by anharmonic interactions, including a large ϕ_{133} stretch-stretch Fermi term,

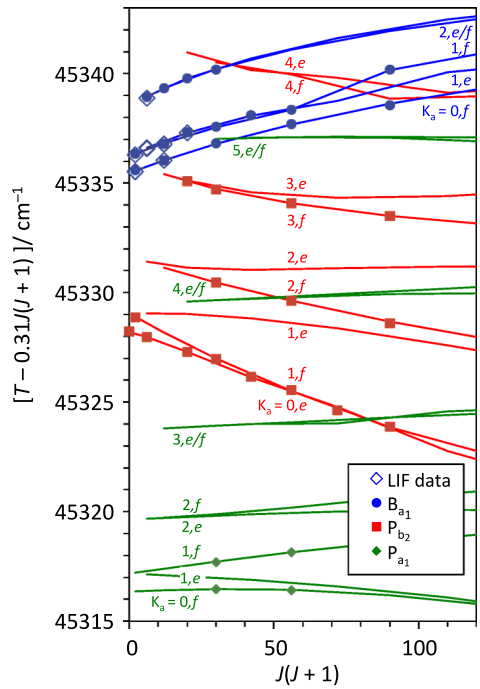

FIG. 6. The observed low-J term energies of C̃-state SO_2 near 45 330 cm^{-1}, reduced by (0.31 cm^{-1})×$J(J+1)$, are plotted against $J(J+1)$. Curves through the data are from the fit given in Table I. Experimental data from the LIF spectrum of Ref. 16, corrected for the calibration offset (see text), are plotted as open diamonds and mmODR data from the current work are plotted as filled circles. The vibrational levels are colored according to the legend.

and the level structure is not fully understood at ~2000 cm^{-1} of vibrational excitation. The vibrational levels in this region are highly mixed in the harmonic basis, and we do not attempt to make harmonic vibrational assignments in the current work.

Throughout this paper, when labeling near prolate asymmetric top rotational transitions, we use a capital letter to denote the change in J and a lower case superscript to denote the change in K_a. The main and subscripted numbers in parentheses are J'' and K_a'' of the lower level, respectively. (For example, $^{q}R_1(6)$ means $K_a' = K_a'' = 1$ and $J' - 1 = J'' = 6$.) Due to oxygen atom nuclear spin statistics in SO_2, only one value of K_c is allowed for a given set of other quantum numbers, so we omit the conventional K_c'' label. In our analysis of the spectra, we use the $\tilde{X}(0,0,0)$ ground state rotational term values from Ref. 27.

After performing a total of six CCPT scans probing different ground state rotational transitions, we were able to obtain 16 rotational term values belonging to P_{b_2} and four rotational term values belonging to P_{a_1}. The term values are listed in the Appendix and a reduced term value plot is shown in Figure 6. The data were fit to an asymmetric top Hamiltonian, including off-diagonal c-axis Coriolis matrix elements between levels of a_1 and b_2 vibrational symmetry. The matrix elements are given by

$$\langle V,J,k|\boldsymbol{H}|V,J,k\rangle = T_0(V) + \left[A - \frac{1}{2}(B+C)\right]k^2 + \frac{1}{2}(B+C)J(J+1), \tag{3}$$

$$\langle V,J,k\pm 2|\boldsymbol{H}|V,J,k\rangle = \frac{1}{4}(B-C)[J(J+1) - k(k\pm 1)]^{1/2}[J(J+1) - (k\pm 1)(k\pm 2)]^{1/2}, \tag{4}$$

$$\langle V',J,k\pm 1|\boldsymbol{H}|V,J,k\rangle = \mp t_1(V',V)[J(J+1) - k(k\pm 1)]^{1/2}. \tag{5}$$

Equations (3)–(4) give diagonal and off-diagonal elements of the rigid rotor Hamiltonian in the prolate symmetric top basis, and Eq. (5) gives the c-axis Coriolis matrix elements connecting levels of a_1 vibrational symmetry to levels of b_2 vibrational symmetry. V labels the vibrational state. The t_1 parameter depends on the vibrational levels, V and V', and replaces $C\zeta_{23}^{(c)}\Omega_{23}(v_2v_3')^{1/2}$ or $C\zeta_{13}^{(c)}\Omega_{23}(v_1v_3')^{1/2}$ in the harmonic expression for the $\zeta_{23}^{(c)}$- or $\zeta_{13}^{(c)}$-type matrix elements, respectively, where we have assumed $V = (v_1, v_2, v_3' - 1)$ and $V' = (v_1 - 1, v_2, v_3')$ or $(v_1, v_2 - 1, v_3')$. However, since the levels considered in the current work are highly anharmonic and the harmonic expansions of these levels are not well known, we treat the vibrational dependence of the matrix elements phenomenologically.

The best fit parameters for the B_{a_1}, P_{b_2}, and P_{a_1} levels are given in Table I. The inertial defects in the rotational constants are all small, indicating that the most significant effects from Coriolis interactions on the rotational constants have probably been deperturbed. (The effective rotational constants reported in Ref. 16 have an inertial defect of −16.3 amu · Å^2.) However, there were significant correlations among the C constants and t_1 Coriolis parameter for the B_{a_1} and P_{b_2} states, so these should be considered "effective" values and caution should be taken in extrapolating the fit to higher J. The average error of the fit was 0.028 cm^{-1}, which is on the order of the calibration uncertainty of our pulsed dye laser.

TABLE I. Fit parameters for the observed interacting levels, B_{a_1}, P_{b_2}, and P_{a_1}. All energies are in cm^{-1} units and the inertial defects (Δ) are listed in amu · Å^2 units. Reported statistical uncertainties are 2σ. There were three correlation coefficients greater than 0.9: between the C constants for the B_{a_1} and P_{b_2} states (−0.96), and between $t_1(B_{a_1},P_{b_2})$ and the C constants for B_{a_1} (0.994), and P_{b_2} (−0.952). No other correlation coefficients were greater than 0.83. The average residual error of the fit was 0.028 cm^{-1}.

	B_{a_1}	P_{b_2}	P_{a_1}
T_0	45 335.44(3)	45 328.21(4)	45 316.42(7)
T_{vib}	2761.99(3)	2754.76(4)	2742.98(7)
A	1.169(7)	1.140(10)	1.09(10)
B	0.3388(27)	0.341(3)	0.340(4)
C	0.280(21)	0.283(18)	0.298(5)
Δ (amu · Å^2)	−0.239	−0.279	−0.502
		$t_1(B_{a_1},P_{b_2}) = 0.43(4)$	
		$t_1(P_{b_2},P_{a_1}) = 0.15(4)$	

The c-axis Coriolis interaction between B_{a_1} and P_{b_2} increases the effective C constant of B_{a_1} and decreases the effective C constant of P_{b_2}. As a result, the e/f asymmetry splitting in P_{b_2} is pronounced, while the e/f splitting in B_{a_1} is very small—in fact, the splitting in the $K_a = 1$ stack of B_{a_1} is reversed at low J leading to a negative value for the apparent $(B - C)/2$ splitting parameter. There is a local perturbation in the $J_{K_aK_c} = 9_{18}$ level of B_{a_1} which appears to be caused by a narrowly avoided crossing between the $K_a = 1$ stack of B_{a_1} and the $K_a = 4$ stack of P_{b_2}.

The frequencies reported in Ref. 16 for the B_{a_1} rotational levels appear to be offset from our measured frequencies by a constant value. Figure 7 shows the energy offset in the measured term energies for the rotational levels assigned in both the LIF spectrum of Ref. 16 and in our mmODR spectra. The spectra of Yamanouchi *et al.* were calibrated in a similar manner to our spectra, using a Te_2 absorption spectrum as a frequency reference. However, our mmODR spectra were taken in short (~20 cm^{-1}) scans and each scan was calibrated individually, so that our calibration is local to the B_{a_1} region. We believe the calibration of Yamanouchi *et al.* may have been interpolated from a long scan of the LIF laser, so that the relative frequency steps are accurate, but the overall local calibration has a small offset. The standard deviation of the

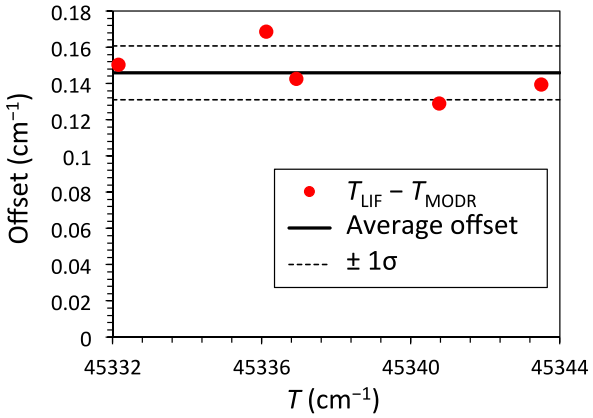

FIG. 7. The difference in the term energies of $\tilde{C}(B_{a_1})$ rotational levels reported in Ref. 16 (T_{LIF}) and in the current work (T_{MODR}) is plotted versus the term energy of levels determined in the current work. The average offset was 0.146 ± 0.0145 cm^{-1}. (The stated uncertainty in the offset is one standard deviation.).

measured offset, 0.0145 cm^{-1}, is approximately the calibration uncertainty of our laser. Therefore, for inclusion in our fitting and in our reduced term value plot (Fig. 6), we have subtracted a 0.146 cm^{-1} offset from the frequencies reported in Ref. 16. The offset affects the band origin reported in Ref. 16, but not the effective rotational constants.

There appears to be a splitting in the $J_{K_aK_c} = 7_{16}$ level of B_{a_1}. Figure 8 shows the ^qP and ^qR transitions to the 7_{16} level, which have nearly identical structure. The most likely explanation is a local perturbation from a dark level, such as

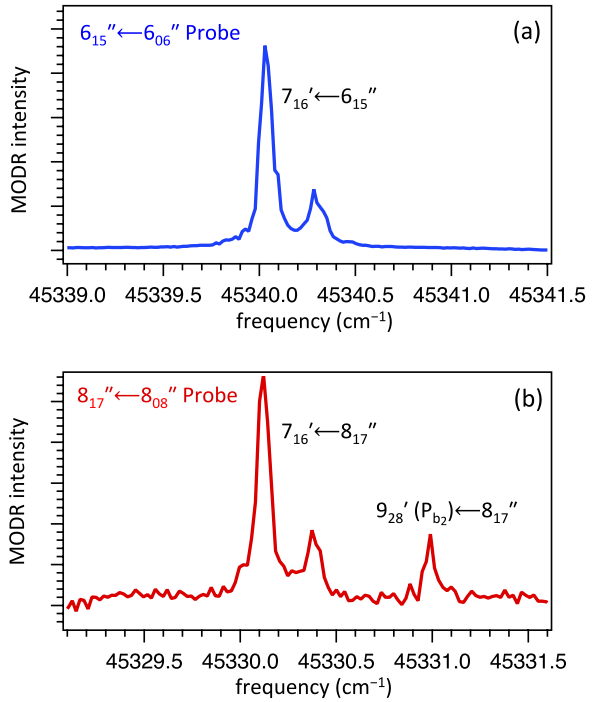

FIG. 8. The $^qR_1(6)$ (panel (a)) and $^qP_1(8)$ (panel (b)) transition to the $J_{K_aK_c} = 7_{16}$ level of $\tilde{C}(B_{a_1})$. The spectra were acquired using the CCPT scheme, probing the $6''_{15} \leftarrow 6''_{06}$ (panel (a)) and the $8''_{17} \leftarrow 8''_{08}$ (panel (b)) rotational transitions of the ground $\tilde{X}(0,0,0)$ level. The nearly identical doublet structure observed in the R and P branches suggests that there is a local perturbation to the $7'_{16}$ level from an otherwise dark state that splits the line. The transition at the right-hand side of panel (b) is to the 9_{28} level of the P_{b_2} band.

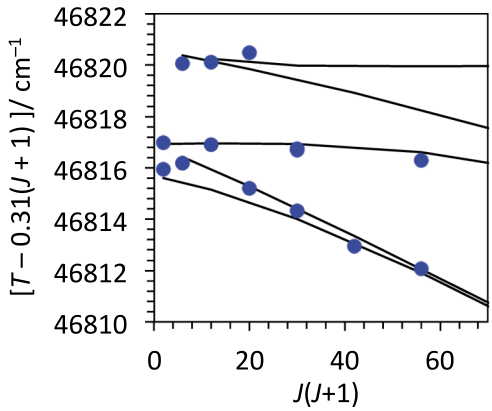

FIG. 9. The observed low-J term energies for the perturbed 46 816 cm^{-1} level, reduced by (0.31 cm^{-1})$\times J(J+1)$, are plotted against $J(J+1)$. Curves through the data are from the effective rotational fit given in Table II.

a triplet state or a highly vibrationally excited level of the $\tilde{X}$ state. In our fit, we have taken the center of gravity of the doublet as the transition frequency.

B. The 46 816 cm^{-1} level

The level at 46 816 cm^{-1} is weak in both the LIF and absorption spectra.[3,16] We performed a Case 1 multiplexed mmODR scan on this band and found that the rotational structure is significantly perturbed. A reduced term value plot is shown in Fig. 9, and the effective rotational fitting parameters to Eqs. (3) and (4) are given in Table II. Due to perturbations, the average error of the fit (0.296 cm^{-1}) was quite large. The depressed effective C constant and large positive inertial defect are suggestive of a c-axis Coriolis interaction with a nearby higher-lying level of b_2 vibrational symmetry. There were a number of extra lines in the spectrum, probably from at least one perturbing vibrational level. However, because the signal-to-noise quality was poor, we did not have enough information to perform a fit to the perturbation.

C. The 47 569 and 47 616 cm^{-1} levels

Because the signal in the mmODR schemes used in the current work depends on the absorption strength of the laser transition rather than the fluorescence intensity, it is an advantageous technique for high-resolution spectroscopy of pre-dissociated levels. The fluorescence intensity from the $\tilde{C}$ state of SO_2 falls off rapidly above the dissociation limit at

TABLE II. Effective rotational fit parameters for the observed vibrational levels at 46 816, 47 569, and 47 616 cm^{-1}. All energies are in cm^{-1} units and the inertial defects (Δ) are listed in amu·Å^2 units. Reported statistical uncertainties are 2σ. $\langle\sigma\rangle$ indicates the average residual error in the fit.

T_0	46 815.6(5)	47 569.328(22)	47 616.08(5)
T_{vib}	4242.2(5)	4995.878(22)	5042.63(5)
A	1.50(16)	1.166(7)	1.124(14)
B	0.36(4)	0.3344(11)	0.3272(24)
C	0.188(17)	0.2730(10)	0.2821(24)
Δ (amu·Å^2)	31.23	−3.109	−6.768
$\langle\sigma\rangle$	0.296	0.0176	0.0382

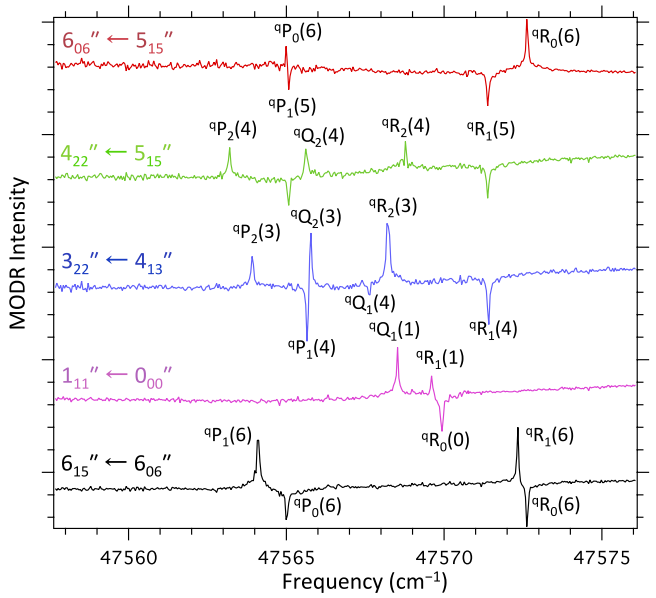

FIG. 10. Case 1 multiplexed mmODR spectrum of the 47 569 cm^{-1} vibrational level of the $\tilde{C}$ state of SO_2. Double resonance signals from five different rotational transitions of the $\tilde{X}(0,0,0)$ ground state (labeled on the left-hand side of the figure) were collected simultaneously in a single scan of the laser. Rotational assignments (shown in the figure) were straightforward due to the population labeling double resonance scheme. Downward and upward directed peaks in the mmODR spectrum represent transitions out of the lower and upper rotational levels of the microwave probe, respectively.

~45 725 cm^{-1}, although the maximum of the Franck-Condon absorption envelope does not occur until ~48 000 cm^{-1}.[3]

In order to demonstrate the effectiveness of the technique for rapid rotational assignment of pre-dissociated levels, we have acquired Case 1 multiplexed mmODR spectra of vibrational levels at 47 569 and 47 616 cm^{-1}, shown in Figs. 10

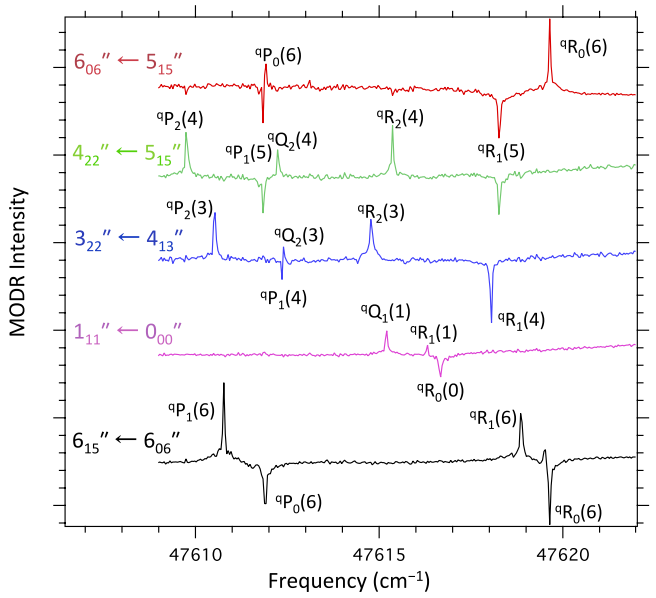

FIG. 11. Case 1 multiplexed mmODR spectrum of the 47 616 cm^{-1} vibrational level of the $\tilde{C}$ state of SO_2. Double resonance signals from five different rotational transitions of the $\tilde{X}(0,0,0)$ ground state (labeled on the left-hand side of the figure) were collected simultaneously in a single scan of the laser. Downward and upward directed peaks in the mmODR spectrum represent transitions out of the lower and upper rotational levels of the microwave probe, respectively.

and 11. Both levels are labeled "(1,9,2)" by Okazaki *et al.*,[3] but we prefer to omit normal mode vibrational assignments for these high-lying levels since the $\tilde{C}$ state is highly anharmonic and the vibrational levels are not well understood at these energies. The 47 569 and 47 616 cm^{-1} vibrational levels have fluorescence quantum yields of 0.0056 and 0.0026 and are weak in the LIF spectrum,[3] but the absorption cross sections of these levels from the $\tilde{X}(0,0,0)$ ground state are roughly 20 times that of the B_{a_1} level, so the transitions are strong in mmODR. Furthermore, the predissociation rate from these levels is 3.40×10^9 and 7.30×10^9 s^{-1},[3] so that the line broadening due to predissociation is on the same order of magnitude as the ~1 GHz bandwidth of our pulsed dye laser and does not lead to significantly problematic broadening of rotational lines.

Reduced term value plots for the 47 569 and 47 616 cm^{-1} levels are shown in Fig. 12. Both levels were fit to the simple rigid rotor asymmetric top Hamiltonian given in Eqs. (3) and (4). The resulting rotational constants are shown in Table II and the fits are plotted in Fig. 12. The rotational structure of the 47 569 cm^{-1} level exhibits no significant perturbations from the rigid rotor Hamiltonian, as evidenced by the 0.0176 cm^{-1} average fit error, which is smaller than the calibration uncertainty (~0.02 cm^{-1}) of our dye laser. On the other hand, the rotational structure of the 47 616 cm^{-1} level provides evidence of a small perturbation, as indicated by the

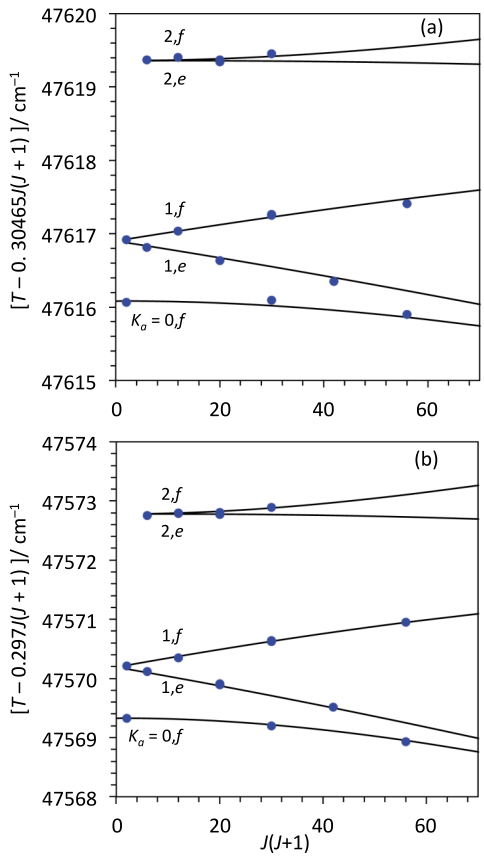

FIG. 12. The observed low-J term energies for the 47 616 cm^{-1} (panel (a)) and 47 569 cm^{-1} (panel (b)) levels, reduced by (0.304 65 cm^{-1})$\times J(J+1)$ and (0.297 cm^{-1})$\times J(J+1)$, respectively, are plotted against $J(J+1)$. Curves through the data are from the fit given in Table II.

small value of $(B - C)/2$ and the fairly large average fit error of 0.0382 cm^{-1}. The perturbation might be from a *c*-axis Coriolis interaction with a lower-lying level of b_2 vibrational symmetry, but it is impossible to be certain without knowing a great deal more about the vibrational level structure in this energy region.

We briefly note the rapid rate of spectral acquisition and unambiguous rotational assignment afforded by the Case 1 multiplexed mmODR technique. Each of the sets of double resonance spectra shown in Figs. 10 and 11 were acquired simultaneously during a ~15 min scan of the pulsed dye laser. Furthermore, the rotational population labeling scheme automates the determination of upper state term energy and in the absence of pathological perturbations, rotational assignment is trivial. The most labor intensive step was frequency calibration via the Te_2 reference spectrum.

IV. DISCUSSION

Because the vibrational level structure of the $\tilde{C}$ state of SO_2 is not yet completely understood in the energy regions investigated in the current work, our fitting parameters should be regarded as "effective." There are clearly perturbations in the levels at 46 816 and 47 616 cm^{-1} that have not been included in the fit. Furthermore, without a better understanding of the level structure, it is difficult to predict whether there are additional perturbers to the B_{a_1} band. If so, it is possible that effects from additional perturbations are folded into the effective constants that we report. If the P_{a_1} band were given the normal mode assignment (1,2,3), then, using $\zeta_{23}^{(c)} = 0.923$ and $C = 0.2654$ cm^{-1},[13] the naive harmonic prediction for the Coriolis interaction strength would be $t_1 = 0.734$ cm^{-1}, which is significantly greater than the 0.43 cm^{-1} interaction strength determined in our fit. The most likely reason for the discrepancy is that, as a result of anharmonicity, many zero-order harmonic basis states contribute to each eigenstate, and it is necessary to sum the harmonic contribution over the full expansion of each eigenstate. Another possibility is that the effects of other perturbations have been folded into the matrix element.

Our results from the $\tilde{C}(B_{a_1})$ region also provide a note of caution to dynamicists investigating vibrational bands that are not fully understood. For example, Zhang and Dai[28] have investigated collisional relaxation of highly vibrationally excited levels of the ground electronic state of SO_2, which couple to the $\tilde{C}$ state and cause quantum beats in the fluorescence decay. They use quantum beats in unassigned rotational lines of the "(1,3,2)" level, but our analysis shows that, for example, the line at 45 329.6 cm^{-1} is actually most likely a transition to the $J_{K_aK_c} = 7_{17}$ level of the P_{b_2} band so that the nominal vibronic symmetry is A_1 rather than B_2. Although we do not believe the conclusions of Zhang *et al.* are incorrect, it can be dangerous to assume vibrational assignments in a perturbed and unanalyzed band.

Ray *et al.*[8] observe dispersed fluorescence from $\tilde{C}$-state levels between 49 000–51 000 cm^{-1} that terminates on $\tilde{X}$-state levels of b_2 vibrational symmetry, and they provide evidence for vibronic coupling of the $\tilde{C}$ state to the dissociative $4\ ^1A'$ electronic state. These authors rule out Coriolis interactions as a source of coupling between levels of A_1 and B_2 vibronic symmetry because they observe strong fluorescence to b_2 levels in a rotationally cold spectrum. However, in the current work, we have observed *c*-axis Coriolis induced transitions to b_2 levels at $J' = 1$. Thus, although there is a strong evidence for vibronic coupling in the vicinity of the avoided crossing,[8,9,29] we do not believe it is possible to rule out Coriolis coupling mechanisms in the $\tilde{C}$ state of SO_2 on the grounds of low rotational temperature. The density of vibrational states at ~8000 cm^{-1} of vibrational excitation is ~0.20/cm^{-1}, or approximately one vibrational level per 5 cm^{-1}. Furthermore, at high vibrational energy, the density of b_2 levels approaches the density of a_1 levels (because both representations are singly degenerate.) As a result, it is statistically very likely that a given a_1 level in this energy region will be within <10 cm^{-1} of the nearest b_2 level, and that there will be significant intensity borrowing through *c*-axis Coriolis matrix elements.

V. CONCLUSIONS AND FUTURE WORK

We have discussed schemes for using frequency-agile technology for generation and detection of millimeter waves (available from our chirped-pulse millimeter wave spectrometer) to improve the state-of-the-art for millimeter-wave optical double resonance spectroscopy. We have demonstrated the use of the multiplexed Case 1 (population labeling) mmODR scheme to obtain a thorough set of low-*J* mmODR spectra, probing many ground state rotational levels simultaneously, in a single scan of the laser. The technique enables rapid spectral acquisition and assignment of congested regions. Our millimeter-wave implementation of the background-free CCPT scheme, originally developed by Twagirayezu and coworkers,[20–22] significantly increases the mmODR sensitivity and allows us to observe weak transitions to levels that perturb the $\tilde{C}(B_{a_1})$ level of SO_2. Due to the relatively short Doppler-dephasing coherence time, we had difficulty implementing a multiplexed CCPT scheme. However, technology for high-power millimeter-wave amplifiers is rapidly advancing, and with higher available power, it will be possible to polarize the transitions faster relative to the coherence dephasing time.

To our knowledge, we also report the first high-resolution observation of a b_2 vibrational level of the $\tilde{C}$ state of SO_2. We have recently acquired IR-UV double-resonance spectra of the low-lying b_2 levels, which will be reported in a future publication,[30] and we are using this data to improve our understanding of the PES and the vibrational dynamics of the $\tilde{C}$ state.[31] Work is also ongoing to analyze the LIF spectrum of the $\tilde{C}(B_{a_1})$ region fully, with the aid of our mmODR spectra.

ACKNOWLEDGMENTS

G.B.P. is grateful for discussions with Brooks Pate, Justin Neill, Adam Steeves, and Kevin Lehmann. This material is based upon work supported by the U.S. Department of Energy, Office of Science, Chemical Sciences Geosciences and Biosciences Division of the Basic Energy Sciences Office, under Award No. DE-FG0287ER13671. We also acknowledge funding from the Camille and Henry Dreyfus Foundation Postdoctoral Program in Environmental Chemistry, and we thank support from NASA Exobiology (Grant No. NNX10AR85G to S.O.).

APPENDIX: LIST OF OBSERVED TERM VALUES

Table III provides a list of term values of assigned rotational levels from the current work.

TABLE III. Rotational term values (T/cm^{-1}) of the C̃-state levels observed in this work.

$J'_{K'_aK'_c}$	T	$J'_{K'_aK'_c}$	T	$J'_{K'_aK'_c}$	T	$J'_{K'_aK'_c}$	T	$J'_{K'_aK'_c}$	T
Vibrational level: P_{a_1}									
$K'_a = 0, f$		$K'_a = 1, f$							
5_{05}	45 325.76	5_{14}	45 327.76						
7_{07}	45 333.78	7_{16}	45 335.50						
Vibrational level: P_{b_2}									
$K'_a = 1, f$		$K'_a = 2, f$		$K'_a = 3, f$		$K'_a = 0, e$		$K'_a = 3, e$	
1_{11}	45 329.51					0_{00}	45 328.22	1_{10}	
5_{15}	45 336.26	5_{24}	45 339.76	5_{33}	45 343.06	2_{02}	45 329.83	3_{12}	
7_{17}	45 342.91	7_{26}	45 346.98	7_{35}	45 344.01	4_{04}	45 333.50	4_{31}	45 341.29
9_{19}	45 351.77	9_{28}	45 356.51	9_{37}	45 351.44	6_{06}	45 339.18	7_{16}	
						8_{08}	45 346.96	9_{18}	
Vibrational level: B_{a_1}									
$K'_a = 0, f$		$K'_a = 1, f$		$K'_a = 2, f$		$K'_a = 1, e$		$K'_a = 2, e$	
1_{01}	45 336.21	1_{10}	45 336.94			2_{12}	45 338.46[a]	2_{21}	45 340.79
3_{03}	45 339.75	3_{12}	45 340.52	3_{21}	45 343.05	4_{14}	45 343.52	4_{23}	45 345.98
5_{05}	45 346.11	5_{14}	45 346.86			6_{16}	45 351.12		
7_{07}	45 355.05	7_{16}	45 355.71					8_{27}	45 363.97
9_{09}	45 366.46	9_{18}	45 368.09						
Vibrational level: 46 816									
$K'_a = 0, f$		$K'_a = 1, f$		$K'_a = 2, f$		$K'_a = 1, e$		$K'_a = 2, e$	
1_{01}	46 816.55	1_{10}	46 817.59			2_{12}	46 818.05	2_{21}	46 821.92
		3_{12}	46 820.62	3_{21}	46 823.83	4_{14}	46 821.39	4_{23}	46 826.68
5_{05}	46 823.63	5_{14}	46 826.02			6_{16}	46 815.07		
7_{07}	46 829.44	7_{16}	46 833.66						
Vibrational level: 47 569									
$K'_a = 0, f$		$K'_a = 1, f$		$K'_a = 2, f$		$K'_a = 1, e$		$K'_a = 2, e$	
1_{01}	47 569.94	1_{10}	47 570.82			2_{12}	47 571.94	2_{21}	47 574.57
		3_{12}	47 573.99	3_{21}	47 576.44	4_{14}	47 575.97	4_{23}	47 578.86
5_{05}	47 578.31	5_{14}	47 579.75	5_{23}	47 582.00	6_{16}	47 582.27		
7_{07}	47 585.93	7_{16}	47 587.95						
Vibrational level: 47 616									
$K'_a = 0, f$		$K'_a = 1, f$		$K'_a = 2, f$		$K'_a = 1, e$		$K'_a = 2, e$	
1_{01}	47 616.67	1_{10}	47 617.53			2_{12}	47 618.64	2_{21}	47 621.20
		3_{12}	47 620.69	3_{21}	47 623.01	4_{14}	47 622.73	4_{23}	47 625.45
5_{05}	47 625.23	5_{14}	47 626.40	5_{23}	47 628.59	6_{16}	47 629.15		
7_{07}	47 632.96	7_{16}	47 634.47						

[a]From Ref. 16, with correction for calibration offset.

[1]S. Becker, C. Braatz, J. Lindner, and E. Tiemann, "Investigation of the predissociation of SO_2: State selective detection of the SO and O fragments," Chem. Phys. **196**, 275–291 (1995).

[2]M. Ivanco, J. Hager, W. Sharfin, and S. C. Wallace, "Quantum interference phenomena in the radiative decay of the ($^1B_2$) state of SO_2," J. Chem. Phys. **78**, 6531 (1983).

[3]A. Okazaki, T. Ebata, and N. Mikami, "Degenerate four-wave mixing and photofragment yield spectroscopic study of jet-cooled SO_2 in the C̃ $^1B_2$ state: Internal conversion followed by dissociation in the X̃ state," J. Chem. Phys. **107**(21), 8752–8758 (1997).

[4]T. Sako, A. Hishikawa, and K. Yamanouchi, "Vibrational propensity in the predissociation rate of SO_2(C̃) by two types of nodal patterns in vibrational wavefunctions," Chem. Phys. Lett. **294**(6), 571–578 (1998).

[5]M. Kawasaki, K. Kasatani, H. Sato, H. Shinohara, and N. Nishi, "Photodissociation of molecular beams of SO_2 at 193 nm," Chem. Phys. **73**(3), 377–382 (1982).

[6]H. Kanamori, J. E. Butler, K. Kawaguchi, C. Yamada, and E. Hirota, "Spin polarization in SO photochemically generated from SO_2," J. Chem. Phys. **83**(2), 611–615 (1985).
[7]K. Kamiya and H. Matsui, "Theoretical studies on the potential energy surfaces of SO_2: Electronic states for photodissociation from the $\tilde{C}\ ^1B_2$ state," Bull. Chem. Soc. Jpn. **64**(9), 2792–2801 (1991).
[8]P. C. Ray, M. F. Arendt, and L. J. Butler, "Resonance emission spectroscopy of predissociating $SO_2\tilde{C}$ (1^1B_2): Coupling with a repulsive $^1A_1$ state near 200 nm," J. Chem. Phys. **109**(13), 5221–5230 (1998).
[9]B. Parsons, L. J. Butler, D. Xie, and H. Guo, "A combined experimental and theoretical study of resonance emission spectra of $SO_2(\tilde{C}^1B_2)$," Chem. Phys. Lett. **320**(5–6), 499–506 (2000).
[10]H. Katagiri, T. Sako, A. Hishikawa, T. Yazaki, K. Onda, K. Yamanouchi, and K. Yoshino, "Experimental and theoretical exploration of photodissociation of SO_2 via the $\tilde{C}^1B_2$ state: Identification of the dissociation pathway," J. Mol. Struct. **413–414**, 589–614 (1997).
[11]B. R. Cosofret, S. M. Dylewski, and P. L. Houston, "Changes in the vibrational population of $SO(^3\Sigma^-)$ from the photodissociation of SO_2 between 202 and 207 nm," J. Phys. Chem. A **104**(45), 10240–10246 (2000).
[12]A. R. Hoy and J. C. D. Brand, "Asymmetric structure and force field of the $^1B_2(^1A')$ state of sulphur dioxide," Mol. Phys. **36**(5), 1409–1420 (1978).
[13]J. C. D. Brand, P. H. Chiu, A. R. Hoy, and H. D. Bist, "Sulfur dioxide: Rotational constants and asymmetric structure of the $\tilde{C}^1B_2$ state," J. Mol. Spectrosc. **60**(1–3), 43–56 (1976).
[14]K.-E. J. Hallin, "Some aspects of the electronic spectra of small triatomic molecules," Ph.D. thesis (The University of British Columbia, 1977).
[15]J. C. D. Brand, D. R. Humphrey, A. E. Douglas, and I. Zanon, Can. J. Phys. **51**, 530 (1973).
[16]K. Yamanouchi, M. Okunishi, Y. Endo, and S. Tsuchiya, "Laser induced fluorescence spectroscopy of the $\tilde{C}^1B_2$–$\tilde{X}^1A_1$ band of jet-cooled SO_2: Rotational and vibrational analyses in the 235–210 nm region," J. Mol. Struct. **352–353**, 541–559 (1995).
[17]G. B. Park, A. H. Steeves, K. Kuyanov-Prozument, J. L. Neill, and R. W. Field, "Design and evaluation of a pulsed-jet chirped-pulse millimeter-wave spectrometer for the 70–102 GHz region," J. Chem. Phys. **135**(2), 24202 (2011).
[18]G. G. Brown, B. C. Dian, K. O. Douglass, S. M. Geyer, S. T. Shipman, and B. H. Pate, "A broadband Fourier transform microwave spectrometer based on microwave chirped pulse excitation," Rev. Sci. Instrum. **79**, 053103 (2008).
[19]B. C. Dian, G. G. Brown, K. O. Douglass, and B. H. Pate, "Measuring picosecond isomerization kinetics via broadband microwave spectroscopy," Science **320**(5878), 924–928 (2008).
[20]S. Twagirayezu, T. N. Clasp, D. S. Perry, J. L. Neill, M. T. Muckle, and B. H. Pate, "Vibrational coupling pathways in methanol as revealed by coherence-converted population transfer Fourier transform microwave infrared double-resonance spectroscopy," J. Phys. Chem. A **114**(25), 6818–6828 (2010).
[21]S. Twagirayezu, X. Wang, D. S. Perry, J. L. Neill, M. T. Muckle, B. H. Pate, and L.-H. Xu, "IR and FTMW-IR spectroscopy and vibrational relaxation pathways in the CH stretch region of CH_3OH and CH_3OD," J. Phys. Chem. A **115**(34), 9748–9763 (2011).
[22]J. L. Neill, K. O. Douglass, B. H. Pate, and D. W. Pratt, "Next generation techniques in the high resolution spectroscopy of biologically relevant molecules," Phys. Chem. Chem. Phys. **13**, 7253–7262 (2011).
[23]A. H. Steeves, H. A. Bechtel, S. L. Coy, and R. W. Field, "Millimeter-wave-detected, millimeter-wave optical polarization spectroscopy," J. Chem. Phys. **123**(14), 141102 (2005).
[24]M. Nakajima, Y. Sumiyoshi, and Y. Endo, "Development of microwave-optical double-resonance spectroscopy using a Fourier-transform microwave spectrometer and a pulsed laser," Rev. Sci. Instrum. **73**(1), 165–171 (2002).
[25]B. C. Dian, K. O. Douglass, G. G. Brown, J. J. Pajski, and B. H. Pate, "Ultraviolet-chirped pulse Fourier transform microwave (UV-CPFTMW) double-resonance spectroscopy," 61st International Symposium on Molecular Spectroscopy, 2006.
[26]See supplementary material at http://dx.doi.org/10.1063/1.4916908 for a comparison spectrum recorded via the CCPT and multiplexed Case 1 MODR techniques.
[27]S. P. Belov, M. Y. Tretyakov, I. N. Kozin, E. Klisch, G. Winnewisser, W. J. Lafferty, and J.-M. Flaud, "High frequency transitions in the rotational spectrum of SO_2," J. Mol. Spectrosc. **191**(1), 17–27 (1998).
[28]M. Zhang and H.-L. Dai, "Quantum state-resolved collision relaxation of highly vibrationally excited SO_2," J. Phys. Chem. A **111**(38), 9632–9639 (2007).
[29]D. Xie, H. Guo, O. Bludský, and P. Nachtigall, "Absorption and resonance emission spectra of $SO_2(\tilde{X}^1A_1/\tilde{C}^1B_2)$ calculated from *ab initio* potential energy and transition dipole moment surfaces," Chem. Phys. Lett. **329**(5–6), 503–510 (2000).
[30]G. B. Park, J. Jiang, C. A. Saladrigas, and R. W. Field, "Direct observation of the low-lying b_2 symmetry vibrational levels of the $\tilde{C}^1B_2$ state of SO_2 by IR-UV double resonance: Characterization of the asymmetry staggering and the origin of unequal bond lengths" (unpublished).
[31]J. Jiang, G. B. Park, and R. W. Field, "Determination of internal force constants of $\tilde{C}$ state SO_2" (unpublished).